



# The Applicability of Green's Theorem to Computation of Rate of Approach

ZORAN DURIC

*Department of Computer Science, George Mason University, Fairfax, VA 22030, USA*

AZRIEL ROSENFELD

*Center for Automation Research, University of Maryland, College Park, MD 20742-3275, USA*

JAMES DUNCAN

*Department of Mechanical Engineering, University of Maryland, College Park, MD 20742-3035, USA*

*Received ; Revised*

**Abstract.** The rate of approach (ROA) of a moving observer toward a scene point, as estimated at a given instant, is proportional to the component of the observer's instantaneous velocity in the direction of the point. In this paper we analyze the applicability of Green's theorem to ROA estimation. We derive a formula which relates three quantities: the average value of the ROA for a surface patch in the scene; a surface integral that depends on the surface slant of the patch; and the contour integral of the normal motion field around the image of the boundary of the patch. We analyze how much larger the ROA on the surface patch can be than the value of the contour integral, for given assumptions about the variability of the distance to points on the surface patch. We illustrate our analysis quantitatively using synthetic data, and we also validate it qualitatively on real image sequences.

**Keywords:** time to collision, rate of approach, Green's theorem

## 1. Introduction

It is well known that the absolute distances of scene points and the magnitude of translational motion cannot both be recovered from an image sequence acquired by a monocular moving observer; only relative distances and the direction of motion are available (Adiv, 1985; Bruss and Horn, 1983; Longuet-Higgins and Prazdny, 1980; Nakayama, 1985). However, the time to contact or collision (TTC) can be found (Lee, 1980) without explicit knowledge of either absolute distances or relative velocities. The TTC for a given scene point is the (apparent) time until (potential) collision of the observer with the point. It is defined as the ratio  $d/v_r$ , where  $d$  is the distance of the point from the observer and  $v_r$  is the relative velocity of approach of the observer to the point. The inverse of the TTC,  $v_r/d$ , is the fraction of the distance  $d$  that the observer traverses

in unit time; it can therefore be regarded as a rate of approach (ROA).

The motion of the observer relative to the scene induces image changes that can be described by an image velocity field, or optical flow field. The projection of the optical flow field onto the field of image gradient directions is called the normal flow field. Several researchers have explored the relationship between the TTC and the divergence (a measure of expansion) of the optical flow or normal flow field (Ancona and Poggio, 1993; Burlina and Chellappa, 1996; Burlina and Chellappa, 1998; Cipolla and Blake, 1992; Francois and Bouthemy, 1990; Maybank, 1987; Meyer and Bouthemy, 1992; Nelson and Aloimonos, 1989; Subbarao, 1990; Tistarelli and Sandini, 1993). They found that the divergence can be decomposed into two terms: one inversely proportional to the TTC and the other a function of the slope of the viewed

surface and the angle between the direction of motion and the viewing direction. In (Koenderink and Van Doorn, 1975; Longuet-Higgins and Prazdny, 1980; Subbarao, 1990) it was shown how the divergence can be computed from the derivatives of the optical flow field. In (Nelson and Aloimonos, 1989) the directional divergence was defined and used for obstacle avoidance. It was computed by taking derivatives of a dense normal flow field obtained from a textured background and textured objects. In (Tistarelli and Sandini, 1993) the polar and logpolar mappings were used to estimate the TTC from normal flow. In (Burlina and Chellappa, 1996) a method of recovering the TTC using spectral operators derived from Mellin transform analysis was presented. This was further generalized in (Burlina and Chellappa, 1998) to detecting the occurrence of, and predicting the time to elapse before, certain kinematic events such as collision or synchronization; accelerated polynomial motion was assumed.

There are potential problems with the stability and accuracy of methods which require computation of the derivatives of a flow field. Fortunately, Green's theorem relates the integral of the optical flow field along an image contour to the integral of the divergence of the field on the surface bounded by the contour. The use of integrals of the field should in principle result in methods that are more accurate and more stable. Several researchers have investigated methods that make use of such integrals. It was shown in (Maybank, 1987) that the rate of change of area, divided by the area, for a small image patch through which the direction of motion passes, is proportional to the divergence of the optical flow field. This result has been generalized to the derivatives of the moments of the patch (Cipolla and Blake, 1992), and has been used to compute the TTC. In (Poggio et al., 1991) Green's theorem was applied to a linear optical flow field. (The optical flow field is linear for constant depth if there is no rotational motion.) The integral of the normal flow along a contour which remains in the center of the visual field and in the direction of motion (i.e., the contour subtends a small angle relative to the direction of motion) has also been used for computation of the TTC (Sharma, 1992).

The accuracy of methods based on integrals of the optical flow or normal flow field has not been analyzed. In particular, there has been no attempt to formulate conditions under which Green's theorem can be used to compute the TTC or the ROA to within a given accuracy. It has been shown (Cipolla and Blake, 1992; Maybank, 1987; Nelson and Aloimonos, 1989;

Sharma, 1992) that the divergence of the optical flow is approximately proportional to the inverse of the TTC (=the ROA) when the partial derivatives of the distance are small or when the contour lies in the direction of motion. However, the meaning of "small" partial derivatives of the distance has not been quantified, nor has it been shown how the computed values change when the contour does not lie in the direction of motion.

In this paper we use Green's theorem to derive an equation which relates the integral of the normal motion field along a closed image contour to the average value of the ROA on a surface patch whose image is bounded by the contour and to a surface integral that depends on the surface slant of the patch. We analyze how much larger the ROA on the surface patch can be than the value of the contour integral, for given assumptions about the variability of the distance to points on the surface patch. We confirm this analysis experimentally using synthetic data and we also validate our approach qualitatively on real image sequences.

## 2. Preliminaries

The analysis presented in this paper makes use of an observer-centered coordinate system and a spherical imaging model. In this section we derive equations for the image velocity field and its divergence in spherical coordinates.

### 2.1. The Spherical Imaging Model

Consider a sphere with the nodal point  $O$  of the camera at its center and with its radius equal to the camera focal length  $f$ ; without loss of generality we can set  $f = 1$  so that the sphere is a unit sphere. This sphere will be called the *image egosphere* (*IE*) (Albus, 1991). Consider a Cartesian coordinate system with origin  $O$  and with positive  $z$ -axis pointing from  $O$  to the north pole  $N$  of the *IE*. Let  $\Pi$  be the plane tangent to the *IE* at  $N$ . If the image of the scene is obtained through plane perspective projection, the image surface is  $\Pi$ ; if the image is obtained through spherical projection, the image surface is the *IE* (see Fig. 1). The perspective projection image of scene point  $(x, y, z)$  is  $(\xi, \eta, 1) = (x/z, y/z, 1)$  and its spherical projection image (see Ikeuchi, 1984) is  $(x/R, y/R, z/R) = (\xi/R_z, \eta/R_z, 1/R_z)$ , where  $R = \sqrt{x^2 + y^2 + z^2}$  and  $R_z = R/z = \sqrt{\xi^2 + \eta^2 + 1}$ .

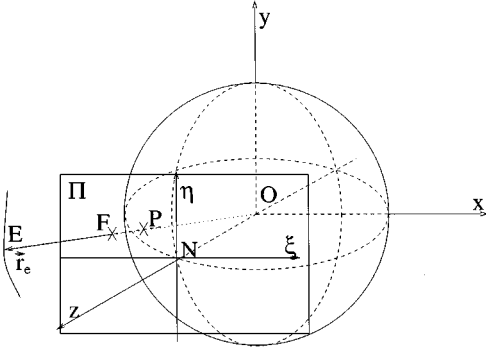


Figure 1. The perspective projection image of scene point  $E = (x, y, z)$  is  $F = (\xi, \eta, 1) = (x/z, y/z, 1)$ ; the spherical projection image of  $E$  is  $P = (x/R, y/R, z/R) = (\xi/R_z, \eta/R_z, 1/R_z)$ , where  $R = \|\vec{r}_e\|$  and  $R_z = R/z$ .

Let  $\vec{r}_e$  be a scene point, and let  $R = \|\vec{r}_e\|$  be its distance from  $O$ . Then  $\vec{r}_e/R$  is a unit vector  $\vec{r}$  from  $O$  to the surface of the  $IE$ . A scene point is defined either by a vector  $\vec{r}_e = (x \ y \ z)^T$  in Cartesian coordinates, or by a triple  $(\rho, \theta, \varphi)$ , in spherical coordinates, where  $\rho = R$ , the latitude  $\theta$  is the angle between  $\vec{r}_e$  and the  $z$ -axis, and the longitude  $\varphi$  is the angle between the  $x$ -axis and the projection of  $\vec{r}_e$  onto the plane  $xOy$ . The unit orthogonal vectors associated with the spherical coordinate system are  $\vec{e}_\theta$ ,  $\vec{e}_\varphi$ , and  $\vec{e}_\rho$ .

## 2.2. The Motion Field and the Optical Flow Field

If the scene is stationary and the observer is moving, the instantaneous velocity  $\dot{\vec{r}}_e$  of scene point  $\vec{r}_e$  relative to the observer (where the dot denotes derivative with respect to time) is given by

$$\dot{\vec{r}}_e = -\vec{T} - \vec{\Omega} \times \vec{r}_e \quad (1)$$

where  $\vec{\Omega}$  is the instantaneous rotational velocity and  $\vec{T}$  is the instantaneous translational velocity; the norm  $\|\vec{T}\|$  of  $\vec{T}$  will be denoted by  $v$ .

The instantaneous velocity of the image point  $\vec{r}$  on the  $IE$  is obtained by taking derivatives of both sides of  $\vec{r} = \vec{r}_e/R$  with respect to time, and using  $\dot{R} = \dot{\vec{r}}_e \cdot \vec{r}_e/R$ :

$$\dot{\vec{r}} = \frac{1}{R}[-\vec{T} + \vec{r}(\vec{T} \cdot \vec{r})] - \vec{\Omega} \times \vec{r}. \quad (2)$$

The first term on the r.h.s. is the *translational motion field*  $\dot{\vec{r}}_t$ , and the second term is the *rotational motion field*  $\dot{\vec{r}}_\omega$ .

We can obtain a simple expression for  $\dot{\vec{r}}_t$  in spherical coordinates by using a coordinate system  $Oxyz$  in which the  $z$ -axis is parallel to  $\vec{T}$ , so that  $\vec{T} = (0 \ 0 \ v)^T$ . In spherical coordinates,  $\dot{\vec{r}}_t$  then becomes

$$\dot{\vec{r}}_t = \frac{v}{\rho} \sin \theta \vec{e}_\theta. \quad (3)$$

If we choose a direction  $\vec{n}_r$  in the image (at the point  $\vec{r}$ ) and call it the normal direction, then the *normal motion field* at  $\vec{r}$  is  $\dot{\vec{r}}_n = (\dot{\vec{r}} \cdot \vec{n}_r)\vec{n}_r$ .  $\vec{n}_r$  can be chosen in various ways; the usual choice is the direction of the image intensity gradient.

## 2.3. The Divergence of the Motion Field

The motion field  $\dot{\vec{r}} = \dot{\vec{r}}_t + \dot{\vec{r}}_\omega$  is a vector field on the surface of the  $IE$ . The divergence of this field is (Marsden and Tromba, 1976)

$$\text{div } \dot{\vec{r}}_t = \frac{v}{\rho} \left( 2 \cos \theta - \frac{\sin \theta}{\rho} \frac{\partial \rho}{\partial \theta} \right), \quad (4)$$

$$\text{div } \dot{\vec{r}}_\omega = 0. \quad (5)$$

*Green's theorem* states (Marsden and Tromba, 1976) that if  $S$  is a two-sided surface patch bounded by a simple closed piecewise smooth curve  $C$ , and the vector field  $\vec{V}$  is everywhere tangent to  $S$  and has continuous derivatives on  $S$ , then

$$\oint_C \vec{V} \cdot \vec{n} \, dl = \iint_S \text{div } \vec{V} \, dS \quad (6)$$

where  $\vec{n}$  is the unit normal to  $C$ ,  $dl$  is an element of  $C$ , and  $dS$  is an element of  $S$ ;  $C$  is traversed in the positive direction (when an observer walks in this direction along  $C$ , and the observer's head points along the positive normal to  $S$ ,  $S$  is on the observer's left.)

## 3. Estimating the Rate of Approach Using Green's Theorem

Let  $S$  be a region on the  $IE$  which is the image of some surface patch  $\Sigma$  in the scene, and let  $C$  be the boundary of  $S$ ; thus  $C$  is the image of a space curve  $\Lambda$  which is the boundary of  $\Sigma$  (see Fig. 2). We assume that  $\Sigma$  is defined by a continuous, single-valued function  $\rho(\theta, \varphi)$  which is almost everywhere differentiable with respect to  $\theta$ .

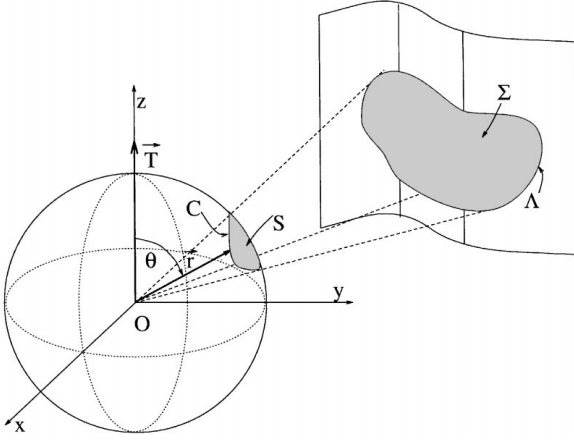


Figure 2. Surface patch  $\Sigma$  bounded by contour  $\Lambda$  projects onto image patch  $S$  bounded by contour  $C$  on the IE.

If we apply (6) to  $\dot{\vec{r}}_\omega$ , using (5), we have

$$\oint_C \dot{\vec{r}}_\omega \cdot \vec{n}_r dl = \iint_S \text{div } \dot{\vec{r}}_\omega dS = 0.$$

Hence when we apply (6) to  $\dot{\vec{r}} = \dot{\vec{r}}_t + \dot{\vec{r}}_\omega$  and use (4), we obtain

$$\oint_C \dot{\vec{r}} \cdot \vec{n}_r dl = \iint_S \frac{2v}{\rho} \cos \theta dS - \iint_S \frac{v \sin \theta}{\rho^2} \frac{\partial \rho}{\partial \theta} dS \quad (7)$$

where  $\vec{n}_r$  is the unit normal to  $C$  at  $\vec{r}$ . If we rewrite  $-\rho^{-2}(\partial \rho / \partial \theta)$  in the second term on the r.h.s. of (7) as  $\partial(\rho^{-1}) / \partial \theta$  and divide both sides of (7) by  $2A_S$ , where  $A_S$  is the area of  $S$ , we obtain

$$\frac{1}{2A_S} \oint_C \dot{\vec{r}} \cdot \vec{n}_r dl = \frac{1}{A_S} \iint_S \frac{v \cos \theta}{\rho} dS + \frac{v}{2A_S} \iint_S \sin \theta \frac{\partial}{\partial \theta} (\rho^{-1}) dS. \quad (8)$$

In what follows we denote the three terms of (8) by  $I_n$ ,  $N_\Sigma$ , and  $D_\Sigma$ , respectively, so that (8) can be written as

$$I_n = N_\Sigma + D_\Sigma. \quad (9)$$

The ROA for a scene point  $\vec{r}_e$  whose spherical coordinates are  $(\rho_r, \theta_r, \phi_r)$  is given by  $v(\vec{r}_e) = v_r / \rho_r$ , where  $v_r$  is the norm of the projection of the translational velocity  $\vec{T}$  onto the viewing direction  $\vec{r}$ . By our choice of coordinate system in Section 2.2, the angle between

$\vec{T}$  and  $\vec{r}$  is  $\theta_r$ ; hence  $v_r = \|\vec{T}\| \cos \theta_r = v \cos \theta_r$  (we recall that  $v$  is the norm of  $\vec{T}$ ), so that

$$v(\vec{r}_e) = \frac{v \cos \theta_r}{\rho_r}.$$

Thus the integrand of  $N_\Sigma$  in (9) is the ROA  $v$  at an arbitrary scene point;  $N_\Sigma$  (“ $N$ ” for “(rate of) nearing”) is thus the average value of  $v$ , averaged over  $S$ , for all scene points which project onto  $S$ , i.e., for all scene points that lie on the surface patch  $\Sigma$ .  $N_\Sigma$  can be either positive (object approaching) or negative (object receding). We will assume the former in our analysis, but the analysis in the reverse case is symmetric.

$I_n$  in (9) is a contour integral along the image contour  $C$ . However, the integrand of  $I_n$  is the normal motion field (or rather its projection on the contour normal  $\vec{n}_r$ ), which is not directly observable in the image. To estimate the integrand we can use the normal flow field  $\vec{u}_n$  in place of the normal motion field  $\dot{\vec{r}}_n$ , since as mentioned at the end of Section 2.2, we have  $\vec{u}_n \approx \dot{\vec{r}}_n$  when the normal direction is collinear with the image gradient direction and the magnitude of the image gradient is large. We will therefore assume here that we can estimate  $I_n$  relatively accurately if the image gradient is high on the contour  $C$  and is normal to the direction of the contour.

$D_\Sigma$  in (9) is a surface integral which depends on the variability of  $\rho$  on  $\Sigma$ . If we can estimate bounds on  $D_\Sigma$ , we can determine how much larger  $v$  (or  $N_\Sigma$ ) can be than the observable quantity  $I_n$ ; note that large values of  $v$  correspond to short times to collision. In Section 4 we will estimate bounds on the ratio  $v/I_n$  for given constraints on the values of  $\theta$  and  $\rho$  on  $\Sigma$ .

#### 4. Accuracy of the Estimate

We assume that the direction of motion  $\theta = 0$  is known;<sup>1</sup> that  $\Sigma$  subtends a relatively small angle (e.g.,  $\Delta\theta < \pi/15$ ); and that  $\Sigma$  is on a near-collision course with the observer (e.g.,  $\theta < \pi/6$ ). We will also assume below that there are bounds on  $\Delta\rho/\rho_{\min}$  (the variability of  $\rho$  relative to the smallest  $\rho$  on  $\Sigma$ ). Using these assumptions, we will derive bounds (especially, upper bounds) on  $v/I_n$ . This will be done in several steps.

In Section 4.1 we will derive an upper bound on  $v(\vec{r}_e)/N_\Sigma$  for any smooth surface patch  $\Sigma$  and any scene point  $\vec{r}_e$  whose latitude is close to the latitudes of the points on  $\Sigma$ . In Section 4.2 we will derive a lower bound on  $I_n/N_\Sigma$  for a special surface patch  $\hat{\Sigma}$

which has the same boundary curve  $\Lambda$  as  $\Sigma$ . Note that  $I_n$  does not depend on  $\Sigma$ , but only on  $\Lambda$  (see the next to last paragraph of Section 3). Hence (9) tells us that  $N_\Sigma + D_\Sigma$  is the same for all  $\Sigma$  that have the same  $\Lambda$ . From (9) we have  $I_n \geq N_\Sigma - |D_\Sigma|$  for any such  $\Sigma$  so that (since  $N_\Sigma > 0$ )

$$\frac{I_n}{N_\Sigma} \geq 1 - \frac{|D_\Sigma|}{N_\Sigma}. \quad (10)$$

In Section 4.2 we construct  $\hat{\Sigma}$ , derive an expression for  $D_{\hat{\Sigma}}$ , and use it to derive a lower bound on  $I_n/N_{\hat{\Sigma}}$ . Finally, in Section 4.3 we use bounds on  $v(\vec{r}_e)/N_{\hat{\Sigma}}$  and  $I_n/N_{\hat{\Sigma}}$  to determine upper bounds on  $v(\vec{r}_e)/I_n$  when  $\vec{r}_e$  is a point on  $\Sigma$ .

#### 4.1. An Upper Bound on $v/N_\Sigma$

We first apply the mean value theorem (Marsden and Tromba, 1976) to the integral expression (see (8)) for  $N_\Sigma$  to obtain

$$N_\Sigma = \frac{v}{A_S} \iint_S \frac{\cos \theta}{\rho} dS = \frac{v}{A_S \rho_\sigma} \iint_S \cos \theta dS$$

where  $\rho_\sigma$  is the distance to some point on  $\Sigma$ . The remaining integral  $\iint_S \cos \theta dS$  is the area  $A_{S^p}$  of the projection of  $S$  onto the equatorial plane of the  $IE$ . By applying the mean value theorem to this integral we obtain  $A_{S^p} = A_S \cos \theta_s$  where  $\theta_s$  is the latitude of some point on  $S$ . Hence we have

$$N_\Sigma = \frac{v}{\rho_\sigma} \cdot \frac{A_{S^p}}{A_S} = \frac{v \cos \theta_s}{\rho_\sigma}. \quad (11)$$

In what follows we will use both of these expressions for  $N_\Sigma$ .

Let us compute the difference between  $N_\Sigma$ , which is the average value of  $v$  on  $\Sigma$ , and  $v$  at an arbitrary point  $\vec{r}_e$  (not necessarily lying on  $\Sigma$ , but for which  $\theta_r$  is close to  $\theta_s$ ). Let the direction to point  $\vec{r}_e$  be  $(\theta_r, \varphi_r)$  and the distance be  $\rho_r$ . Then

$$v(\vec{r}_e) - N_\Sigma \equiv \frac{v \cos \theta_r}{\rho_r} - \frac{v \cos \theta_s}{\rho_\sigma}. \quad (12)$$

The Taylor series expansion of  $\cos \theta_r$  in the neighborhood of  $\theta_s$  is given by

$$\cos \theta_r = \cos \theta_s - (\theta_r - \theta_s) \sin \theta_s - 0.5(\theta_r - \theta_s)^2 \cos \theta_s$$

where  $\theta_i$  is an angle between  $\theta_s$  and  $\theta_r$ . Using this expansion of  $\cos \theta_s$ , (11), and (12) and rearranging we obtain

$$\frac{v(\vec{r}_e)}{N_\Sigma} = \frac{\rho_\sigma}{\rho_r} \left[ 1 - (\theta_r - \theta_s) \tan \theta_s - \frac{1}{2} (\theta_r - \theta_s)^2 \frac{\cos \theta_i}{\cos \theta_s} \right].$$

For any  $\theta < \pi/2$  (the observer is moving towards the surface) we have  $\cos \theta_i, \cos \theta_s \geq 0$ , so that the third term inside the square brackets is always negative; hence

$$\frac{v(\vec{r}_e)}{N_\Sigma} < \frac{\rho_\sigma}{\rho_r} (1 + |\theta_r - \theta_s| \tan \theta_s). \quad (13)$$

This is our desired upper bound on  $v/N_\Sigma$ . Note that in deriving this bound we used only the mean value theorem (which requires only that  $\Sigma$  be continuous) and the assumption that  $\theta_r$  is close to  $\theta_s$  and both are  $< \pi/2$  (at the beginning of Section 4 we in fact assumed  $\theta < \pi/6$ ). Hence we can apply (13) to any surface patch  $\Sigma$  and any point  $\vec{r}_e$  that satisfy these assumptions. In particular, in Section 4.3 we will apply it to the surface patch  $\hat{\Sigma}$  that will be constructed in Section 4.2, and to a point  $\vec{r}_e$  of  $\Sigma$ .

#### 4.2. A Lower Bound on $I_n/N_{\hat{\Sigma}}$

In this section we construct the special surface patch  $\hat{\Sigma}$  and derive a lower bound on  $I_n/N_{\hat{\Sigma}}$ . In Section 4.2.1 we construct  $\hat{\Sigma}$ , in Section 4.2.2 we evaluate  $D_{\hat{\Sigma}}$ , and in Section 4.2.3 we use (10) to derive the desired lower bound.

**4.2.1. The Surface Patch  $\hat{\Sigma}$ .** In this section we construct a surface patch  $\hat{\Sigma}$ , having the given boundary curve  $\Lambda$ , on which  $\rho^{-1}$  is linear in  $\theta$ . Specifically,  $\hat{\Sigma}$  will be constructed out of arcs of the form  $\rho^{-1} = a\theta + b$  where  $a$  and  $b$  are constants.

In order to define the arcs from which  $\hat{\Sigma}$  will be constructed, we first segment the contour  $C$  into parts  $C^+$  and  $C^-$  for which the projections of the normal motion field onto the contour normal (i.e.,  $\vec{r}_n \cdot \vec{n}_r$ ) are positive and negative, respectively. For simplicity we assume that, as shown in Fig. 3(a), both  $C^+$  and  $C^-$  are connected, and that  $\theta$  is a one-valued function of  $\varphi$  on both  $C^+$  and  $C^-$ ; we denote these functions by  $\theta^+(\varphi)$  and  $\theta^-(\varphi)$  respectively. Hence  $\rho$  is also a one-valued function of  $\varphi$  on  $C^+$  and  $C^-$ ; we denote these functions by  $\rho^+(\varphi)$  and  $\rho^-(\varphi)$ . Figure 3(a) shows a case in which the direction of motion (which we recall is the direction  $\theta = 0$ , i.e., the north pole  $N$  of the  $IE$ )

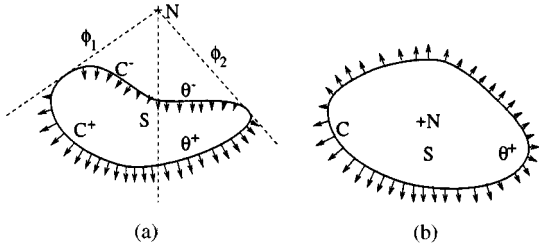


Figure 3. (a) Contour  $C$  in a case where the direction of motion  $\theta = 0$  (the north pole  $N$  of the  $IE$ ) is outside  $C$ . The projection of the normal motion field onto the contour normals is positive along  $C^+$  and negative along  $C^-$ . (b) A case where the direction of motion is inside  $C$ ; here  $C = C^+$ .

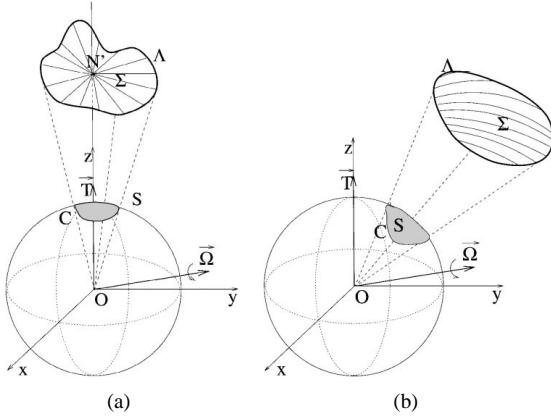


Figure 4. Construction of  $\hat{\Sigma}$ . (a)  $N$  is inside  $S$ . (b)  $N$  is outside  $S$ .

is outside  $C$ ; in this case  $\varphi$  varies over a range  $[\phi_1, \phi_2]$  on both  $C^+$  and  $C^-$ . If  $N$  is inside  $C$ , we have  $C = C^+$  and  $\varphi \in [0, 2\pi]$  on  $C^+$  (see Fig. 3(b)).

Let  $\Pi_\varphi$  be a half-plane bounded by the  $z$ -axis; on any such half-plane,  $\varphi$  has constant value (i.e., the half-plane cuts the  $IE$  in the meridian of longitude  $\varphi$ ). We have just assumed that each  $\Pi_\varphi$  intersects  $S$  in at most one connected arc (so that it intersects  $C$  (and  $\Lambda$ ) in at most two points, the endpoints of this arc). If  $N$  is inside  $C$  the arcs all pass through a common point, which we denote by  $N'$  in Fig. 4(a). If  $N$  is outside  $C$ , the arcs do not intersect, as shown in Fig. 4(b).

Suppose first that  $N$  is inside  $C$  (Fig. 4(a)); then we construct  $\hat{\Sigma}$  by choosing a point  $N' = (\rho_n, 0, 0)$  on the positive  $z$ -axis and joining it to the points of  $\Lambda$  by arcs of the form

$$\frac{1}{\rho} = \frac{1}{\rho_n} + \left( \frac{1}{\rho^+(\varphi)} - \frac{1}{\rho_n} \right) \frac{\theta}{\theta^+(\varphi)}. \quad (14)$$

By our assumptions about  $\Sigma$  (and hence about  $\Lambda$ ), these arcs change continuously as  $\varphi$  changes; thus the arcs

sweep out a surface patch  $\hat{\Sigma}$  whose boundary is  $\Lambda$  and which is continuous everywhere except possibly at  $N'$ .

If  $N$  is outside  $C$  (Fig. 4(b)) we construct  $\hat{\Sigma}$  by joining pairs of points on  $\Lambda$ . Let  $\Pi_\varphi$  intersect  $\Lambda$  at the points  $(\rho^-(\varphi), \theta^-(\varphi), \varphi)$  and  $(\rho^+(\varphi), \theta^+(\varphi), \varphi)$ ; then the arc joining these points is of the form

$$\frac{1}{\rho} = \frac{1}{\rho^-(\varphi)} + \left( \frac{1}{\rho^+(\varphi)} - \frac{1}{\rho^-(\varphi)} \right) \frac{\theta - \theta^-(\varphi)}{\theta^+(\varphi) - \theta^-(\varphi)}. \quad (15)$$

By our assumptions about  $\Sigma$  and  $\Lambda$ , these arcs change continuously as  $\varphi$  changes; thus the arcs sweep out a continuous surface patch  $\hat{\Sigma}$  whose boundary is  $\Lambda$ .

**4.2.2. Evaluation of  $D_{\hat{\Sigma}}$ .** We recall from (8) that  $D_\Sigma$  (and in particular,  $D_{\hat{\Sigma}}$ ) is given by the integral expression

$$\frac{v}{2A_S} \iint_S \sin \theta \frac{\partial}{\partial \theta} (\rho^{-1}) dS$$

where for  $D_{\hat{\Sigma}}$ ,  $\rho^{-1}$  is given by (14) or (15).

In the case of  $N$  inside  $C$ , where  $\rho^{-1}$  is given by (14), we shall now show that there exists a  $\rho_n$  in the range of values of  $\rho^+(\varphi)$  such that  $D_{\hat{\Sigma}} = 0$ . Indeed, in this case we have from (14)

$$\begin{aligned} D_{\hat{\Sigma}} &= \frac{v}{2A_S} \iint_S \left( \frac{1}{\rho^+(\varphi)} - \frac{1}{\rho_n} \right) \frac{\sin \theta}{\theta^+(\varphi)} dS \\ &= \frac{v}{2A_S} \int_0^{2\pi} \left( \frac{1}{\rho^+(\varphi)} - \frac{1}{\rho_n} \right) \\ &\quad \times \frac{1}{\theta^+(\varphi)} \int_0^{\theta^+(\varphi)} \sin^2 \theta d\theta d\varphi \end{aligned}$$

Let

$$\bar{s}(\varphi) = \frac{1}{\theta^+(\varphi)} \int_0^{\theta^+(\varphi)} \sin^2 \theta d\varphi;$$

then

$$\begin{aligned} D_{\hat{\Sigma}} &= \frac{v}{2A_S} \int_0^{2\pi} \left( \frac{1}{\rho^+(\varphi)} - \frac{1}{\rho_n} \right) \bar{s}(\varphi) d\varphi \\ &= \frac{v}{2A_S} \left( \int_0^{2\pi} \frac{\bar{s}(\varphi)}{\rho^+(\varphi)} d\varphi - \frac{1}{\rho_n} \int_0^{2\pi} \bar{s}(\varphi) d\varphi \right). \end{aligned}$$

Thus we can set  $D_{\hat{\Sigma}} = 0$  and solve for  $\rho_n$ , obtaining

$$\rho_n = \left( \int_0^{2\pi} \bar{s}(\varphi) d\varphi \right) \cdot \left( \int_0^{2\pi} \frac{\bar{s}(\varphi)}{\rho^+(\varphi)} d\varphi \right)^{-1}.$$

If we apply the mean value theorem to the second integral on the r.h.s. of this expression<sup>2</sup> we obtain  $\rho_n = \rho^+(\varphi_0)$  for some  $\varphi_0 \in [0, 2\pi]$ . This shows that the  $\rho_n$  for which  $D_{\hat{\Sigma}} = 0$  is indeed in the range of values of  $\rho^+(\varphi)$ .

In the case of  $N$  outside  $C$ ,  $\rho^{-1}$  is given by (15), and we similarly have

$$D_{\hat{\Sigma}} = \frac{v}{2A_S} \int_{\phi_1}^{\phi_2} \left( \frac{1}{\rho^+(\varphi)} - \frac{1}{\rho^-(\varphi)} \right) \times \frac{1}{\theta^+(\varphi) - \theta^-(\varphi)} \int_{\theta^-(\varphi)}^{\theta^+(\varphi)} \sin^2 \theta \, d\theta \, d\varphi. \quad (16)$$

Let

$$\tilde{s}(\varphi) = \frac{1}{\theta^+(\varphi) - \theta^-(\varphi)} \int_{\theta^-(\varphi)}^{\theta^+(\varphi)} \sin^2 \theta \, d\theta.$$

If we use

$$\begin{aligned} \sin^2 \theta^-(\varphi) \int_{\theta^-(\varphi)}^{\theta^+(\varphi)} d\theta &\leq \int_{\theta^-(\varphi)}^{\theta^+(\varphi)} \sin^2 \theta \, d\theta \\ &\leq \sin^2 \theta^+(\varphi) \int_{\theta^-(\varphi)}^{\theta^+(\varphi)} d\theta \end{aligned}$$

we obtain

$$0 < \sin^2 \theta^-(\varphi) \leq \tilde{s}(\varphi) \leq \sin^2 \theta^+(\varphi).$$

If we apply the mean value theorem to the integral on the r.h.s. of (16) we obtain

$$D_{\hat{\Sigma}} = \frac{v}{A_S} \left( \frac{1}{\rho^+(\varphi_1)} - \frac{1}{\rho^-(\varphi_1)} \right) \cdot \frac{1}{2} \int_{\phi_1}^{\phi_2} \tilde{s}(\varphi) \, d\varphi$$

for some  $\varphi_1 \in [\phi_1, \phi_2]$ . To evaluate the integral in this expression, consider the region  $S_1$  ( $S_2$ ) on the  $IE$  bounded by the curve  $C_1$  ( $C_2$ ) whose equation is  $\theta = \theta^-(\varphi)$  ( $\theta = \theta^+(\varphi)$ ) and by the meridians of longitude  $\phi_1$  and  $\phi_2$ . Let  $S_1^p$  ( $S_2^p$ ) be the projection of  $S_1$  ( $S_2$ ) onto the equatorial plane of the  $IE$ . Thus  $S_1^p$  ( $S_2^p$ ) is the region bounded by the rays in directions  $\varphi = \phi_1$  and  $\phi_2$  and by the curve whose radius in direction  $\varphi$  is  $\sin \theta^-(\varphi)$  ( $\sin \theta^+(\varphi)$ ) (see Fig. 5).

Therefore, using the standard formula for area in polar coordinates, the area of  $S_1^p$  is given by

$$A_{S_1^p} = \frac{1}{2} \int_{\phi_1}^{\phi_2} \sin^2 \theta^-(\varphi) \, d\varphi. \quad (17)$$

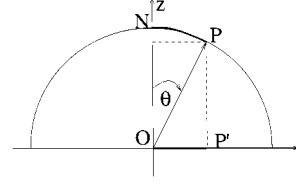


Figure 5. Let  $P = (1, \theta, \varphi)$  be any point on the  $IE$ ; then arc  $NP$  projects onto the line segment  $OP'$  in the equatorial plane, where  $|OP'| = \sin \theta$ .

We thus have

$$D_{\hat{\Sigma}} = v \cdot \frac{\rho^-(\varphi_1) - \rho^+(\varphi_1)}{\rho^-(\varphi_1)\rho^+(\varphi_1)} \cdot \frac{A_{\tilde{S}^p}}{A_S} \quad (18)$$

for some  $A_{\tilde{S}^p}$  such that  $A_{S_1^p} \leq A_{\tilde{S}^p} \leq A_{S_2^p}$ .

**4.2.3. The Lower Bound on  $I_n/N_{\hat{\Sigma}}$ .** From (11) (applied to  $\hat{\Sigma}$ ; see the end of Section 4.1) we have

$$N_{\hat{\Sigma}} = \frac{v}{\hat{\rho}} \cdot \frac{A_{S^p}}{A_S} = \frac{v \cos \theta_s}{\hat{\rho}} \quad (19)$$

where  $\hat{\rho}$  is the distance to some point on  $\hat{\Sigma}$ ; note that by our construction it is also the distance to some point on  $\Lambda$ . In the case of  $N$  inside  $C$  we have  $D_{\hat{\Sigma}} = 0$  and therefore  $I_n \equiv N_{\hat{\Sigma}}$ ; in this case we know the value of  $I_n/N_{\hat{\Sigma}}$  ( $=1$ ) and have no need for a lower bound.

In the case of  $N$  outside  $C$  we have from (18) and (19)

$$\frac{D_{\hat{\Sigma}}}{N_{\hat{\Sigma}}} = \hat{\rho} \cdot \frac{\rho^-(\varphi_1) - \rho^+(\varphi_1)}{\rho^-(\varphi_1)\rho^+(\varphi_1)} \cdot \frac{A_{\tilde{S}^p}}{A_{S^p}}. \quad (20)$$

From (20) and the fact that  $A_{S_1^p} \leq A_{\tilde{S}^p} \leq A_{S_2^p}$  we thus obtain

$$\frac{|D_{\hat{\Sigma}}|}{N_{\hat{\Sigma}}} < \hat{\rho} \cdot \frac{|\rho^-(\varphi_1) - \rho^+(\varphi_1)|}{\rho^-(\varphi_1)\rho^+(\varphi_1)} \cdot \frac{A_{S_2^p}}{A_{S^p}}.$$

Substituting this into (10) gives the desired lower bound on  $I_n/N_{\hat{\Sigma}}$ :

$$\frac{I_n}{N_{\hat{\Sigma}}} > 1 - \hat{\rho} \cdot \frac{|\rho^-(\varphi_1) - \rho^+(\varphi_1)|}{\rho^-(\varphi_1)\rho^+(\varphi_1)} \cdot \frac{A_{S_2^p}}{A_{S^p}}. \quad (21)$$

#### 4.3. How Accurate is $I_n$ as an Estimate of $v$ for Points on $\Sigma$ ?

In the case where the direction of motion is inside  $C$ , we can now use the results of Sections 4.1 and 4.2 to

compute an upper bound on  $v(\vec{r}_e)/I_n$ . Indeed, in this case, as already pointed out,  $I_n = N_{\hat{\Sigma}}$ . Moreover, since (13) holds for  $\vec{r}_e$  and  $\hat{\Sigma}$  (see the end of Section 4.1), we can write

$$\frac{v(\vec{r}_e)}{I_n} = \frac{v(\vec{r}_e)}{N_{\hat{\Sigma}}} < \frac{\hat{\rho}}{\rho_r} (1 + |\theta_r - \theta_s| \tan \theta_s) \quad (22)$$

where  $\theta_r$  and  $\rho_r$  are the latitude and distance of  $\vec{r}_e$ ;  $\theta_s$  is the latitude of some point of  $S$ ; and  $\hat{\rho}$  is the distance of some point on  $\hat{\Sigma}$ . (Note that since the direction of motion  $\theta = 0$  is inside  $C$ , our assumption that  $\Delta\theta < \pi/15$  also implies that  $\theta < \pi/15$ . Thus  $\theta_s < \pi/15$  and  $|\theta_r - \theta_s| < \pi/15$ ; hence  $v(\vec{r}_e)/I_n < [1 + (\pi/15) \tan(\pi/15)] \hat{\rho}/\rho_r < 1.045 \hat{\rho}/\rho_r$ .)

We now assume that the relative distance  $\Delta\rho$  of any two points on  $\Sigma$  is much smaller than the minimal distance  $\rho_{\min}$  of  $\Sigma$ , say  $|\Delta\rho| < \alpha\rho_{\min}$  where  $\alpha \ll 1$ . This assumption also holds for  $\hat{\Sigma}$ , since the range of distances to points on  $\hat{\Sigma}$  is the same as the range of distances to points on  $\Lambda$  (see Section 4.2), and  $\Lambda$  is a subset of  $\Sigma$ . We assume that it also holds for the point  $\vec{r}_e$ —e.g., this is true if  $\vec{r}_e$  lies on  $\Sigma$ . We then have  $\hat{\rho} \equiv \rho_{\min} + \Delta\rho \leq \rho_r + |\Delta\rho| < \rho_r + \alpha\rho_{\min} \leq \rho_r + \alpha\rho_r = (1 + \alpha)\rho_r$ ; in other words, if  $\rho$  can vary only by  $\alpha$ , the amount by which  $v(\vec{r}_e)$  can exceed  $I_n$  is also on the order of  $\alpha$ . (For example, if  $\alpha = 0.1$ , we have  $v(\vec{r}_e)/I_n < (1.045)(1.1) < 1.15$ ; in other words, if  $\rho$  varies by at most 10% on  $\Sigma$  and we use  $I_n$  to estimate  $v$ , the actual (maximum) value of  $v$  exceeds the estimate by less than 15%.)

The situation is more complicated in the case where the direction of motion is outside  $C$ . Here (13) still gives us an upper bound on  $v(\vec{r}_e)/N_{\hat{\Sigma}}$ , and (21) gives us a lower bound on  $I_n/N_{\hat{\Sigma}}$ , but we cannot simply divide the first bound by the second to obtain an upper bound on  $v/I_n$ , because the second bound may be negative. On the other hand, we can show that this bound is positive unless the ratio of areas  $A_{S_2^p}/A_{S^p}$  is quite large. Indeed, our assumption that  $\Delta\rho < \alpha\rho_{\min}$  implies that the expression involving  $\rho$ 's on the r.h.s. of (21) is less than  $\alpha$ . [**Proof:** Without loss of generality, let  $\rho^-(\varphi_1) = a$ ,  $\rho^+(\varphi_1) = a + \delta$ , where  $\delta \geq 0$ ; then the expression becomes  $\hat{\rho}\delta/a(a + \delta)$ . Evidently, for any  $\delta$ ,  $\delta/a(a + \delta)$  takes on its largest possible value when  $a = \rho_{\min}$ . Moreover, for any  $a$ ,  $\delta/a(a + \delta)$  takes on its largest possible value when  $\delta$  is as large as possible; by our assumptions about  $\rho$ , we have  $\delta \leq \Delta\rho < \alpha\rho_{\min}$ . Finally,  $\hat{\rho} \leq \rho_{\min} + \Delta\rho < \rho_{\min}(1 + \alpha)$ . Hence the expression  $< \rho_{\min}(1 + \alpha)\alpha\rho_{\min}/\rho_{\min}(\rho_{\min} + \alpha\rho_{\min}) = \alpha$ .] Thus the r.h.s. of (21) will be positive unless

$A_{S_2^p}/A_{S^p} > 1/\alpha$ . As we see from Fig. 3(a), this can only happen when region  $S$  is small and lies relatively far from the direction of motion. [If  $\alpha = 0.1$ , we are safe as long as  $A_{S_2^p}/A_{S^p} < 10$ . Actually, we could even use an  $\alpha$  smaller than 0.1, since the variability of  $\rho$  on  $\hat{\Sigma}$  (which is the same as the variability on  $\Lambda$ ) should be less than its variability on  $\Sigma$  (because  $\Sigma$  may have internal ‘‘bulges’’ that do not affect its boundary curve  $\Lambda$ ). If we use  $\alpha = 0.05$  instead of  $\alpha = 0.1$ , we are safe as long as  $A_{S_2^p}/A_{S^p} < 20$ —a very large ratio.]

The actual bounds on  $\theta$  and  $\Delta\theta$ , and the actual size of  $A_{S_2^p}/A_{S^p}$ , are observable from the image, and so is  $\cos \theta_s = A_{S^p}/A_S$ . Thus in general, we can judge how good  $I_n$  is as an estimate of  $v$ , for given assumptions about the variability of  $\rho$  on  $\Sigma$  and on  $\Lambda$ , by examining the image. If we denote the variabilities of  $\rho$  on  $\Sigma$  and  $\Lambda$  by  $\alpha_\sigma$  and  $\alpha_\lambda$ , respectively, then when the direction of motion is inside  $C$ , (22) gives us

$$\frac{v(\vec{r}_e)}{I_n} < (1 + \alpha_\sigma) \cdot (1 + \Delta\theta_m \tan \theta_s) \quad (23)$$

(where  $\Delta\theta_m$  is the maximum of latitude difference  $|\theta_r - \theta_s|$  on  $S$ ); and when it is outside  $C$ , (21) and (22) give us

$$\frac{v(\vec{r}_e)}{I_n} < \frac{1 + \alpha_\sigma}{1 - \alpha_\lambda \cdot A_{S_2^p}/A_{S^p}} \cdot (1 + \Delta\theta_m \tan \theta_s). \quad (24)$$

These formulas provide upper bounds on the ratio  $v(\vec{r}_e)/I_n$  as functions of the  $A$ 's and  $\theta$ 's for the given image contour, and of the  $\alpha$ 's (the assumed distance variabilities) for the space curve and surface patch. In the next section we will give numerical examples that illustrate the behavior of these bounds.

## 5. Numerical Examples and Discussion

In this section we examine the behavior of  $v(\vec{r}_e)/I_n$  and of the bounds in (23–24) using a set of numerical examples. In all of these examples  $\Sigma$  is a planar patch, say in the plane  $\Pi_\Sigma$ , and  $\Lambda$  is a circle (see Fig. 6). Let the ray  $OZ$  to the center of  $\Lambda$  meet the  $IE$  at  $(\theta_z, \varphi_z)$ ; in our examples we use  $0^\circ \leq \theta_z \leq 30^\circ$  and (arbitrarily)  $\varphi_z = 0$ .  $\Lambda$  is then determined by its radius and by the orientation of  $\Pi_\Sigma$ . We consider two sets of cases:

1. The normal  $\vec{n}_\sigma$  to  $\Pi_\Sigma$  at  $Z$  is in the plane  $\Pi_0$  of the great circle  $\varphi = 0$ , and makes angle  $\psi_z$  with the ray  $OZ$ ; in our examples we use  $\psi_z = 0^\circ, \pm 30^\circ, \pm 45^\circ$ , and  $\pm 60^\circ$ .

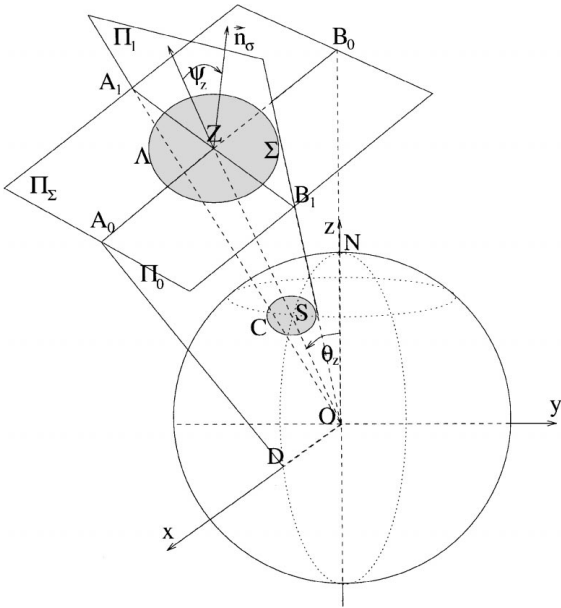


Figure 6.  $\Lambda$  is a circle centered at the point  $Z$  and embedded in the plane  $\Pi_\Sigma$ . The normal  $\vec{n}_\sigma$  of  $\Pi_\Sigma$  lies either in the plane  $\Pi_0$  ( $ODA_0ZB_0$ ) or in the plane  $\Pi_1$  ( $OA_1ZB_1$ ) orthogonal to  $\Pi_0$ .

2. The normal  $\vec{n}_\sigma$  is in the plane  $\Pi_1$  containing  $OZ$  and perpendicular to  $\Pi_0$ , and makes angle  $30^\circ$ ,  $45^\circ$ , or  $60^\circ$  with  $OZ$  (here, by symmetry, the sign of the angle does not matter).

When  $\psi_z = 0$ ,  $C$  is a circle; in our examples, we use circles that subtend angles  $2^\circ$ ,  $6^\circ$ , and  $12^\circ$  at  $O$ , giving us a total of 30 cases (three for each of the ten choices of  $\psi_z$ ). For the nonzero values of  $\psi_z$ ,  $C$  becomes increasingly elongated. Note that in all cases, the direction of motion is inside  $C$  when  $\theta_z = 0$ , but is outside  $C$  when  $\theta_z$  is sufficiently large.

For each case, and for any value of  $\theta_z$ , we can generate the normal motion field (for any speed  $v$ ; we use  $v = 1$  here) and compute  $I_n$ ; and we can also compute the maximum value  $v_m$  of  $v(\vec{r}_z)$  (corresponding to the minimum TTC). In Figs. 7–9 we plot the ratio  $R = v_m/I_n$ , as a function of  $\theta_z$ , for each of our 30 cases. Figures 7 and 8 show the cases in which the normal  $\vec{n}_\sigma$  of  $\Sigma$  is in  $\Pi_0$  (with  $\psi_z$  positive and negative, respectively), and Fig. 9 shows the cases in which it is in  $\Pi_1$ ; for ease of comparison, the common cases  $\psi_z = 0$  are plotted in all three figures. The numbers 1, 3, 6 represent the subtended half-angles  $1^\circ$ ,  $3^\circ$ , and  $6^\circ$ .

We see from Figs. 7–9 that for  $\psi_z = 0$ ,  $R$  increases very slowly with  $\theta_z$ , and remains in the interval  $[1, 1.06]$ ; in other words, when  $\psi_z = 0$ ,  $I_n$

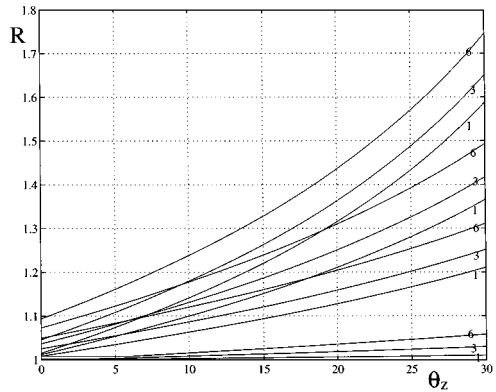


Figure 7. The ratio  $R = v_m/I_n$  for nonnegative values of  $\psi_z$  in the plane  $\Pi_0$ . The groups of curves labeled 1, 3, 6, from bottom to top, are for  $\psi_z = 0^\circ, 30^\circ, 45^\circ$ , and  $60^\circ$ .

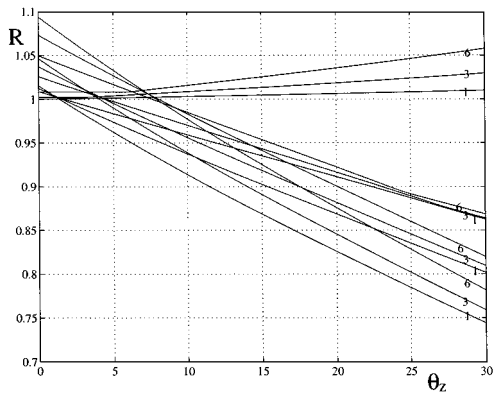


Figure 8. The ratio  $R = v_m/I_n$  for nonpositive values of  $\psi_z$  in the plane  $\Pi_0$ . The groups of curves labeled 1, 3, 6, from top to bottom, are for  $\psi_z = 0^\circ, -30^\circ, -45^\circ$ , and  $-60^\circ$ .

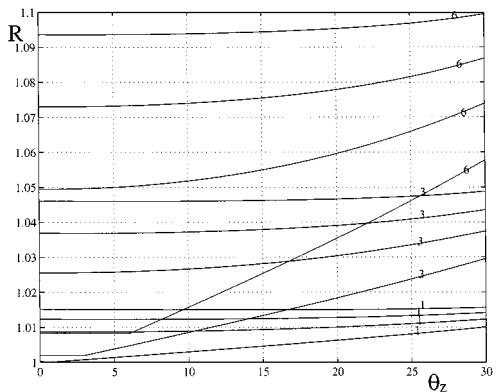


Figure 9. The ratio  $R = v_m/I_n$  for  $\psi_z$ 's in the plane  $\Pi_1$ . The four curves labeled 6, from bottom to top, are for  $\psi_z = 0^\circ, 30^\circ, 45^\circ$ , and  $60^\circ$ , and similarly for the curves labeled 3 and 1.

is a very good estimate of  $v_m$ . This is because  $\Lambda$  is not on a slanted surface, which implies that  $D_\Sigma$  (in Eqs. (8) and (9)) is approximately 0. Figure 9 shows that  $R$  also remains quite small (in the interval [1, 1.1]) when  $\Lambda$  is slanted “sideways”; this is because  $D_\Sigma$  is still small, since the distance to  $\Sigma$  does not change rapidly with  $\theta$ . In these cases  $R$  increases significantly with  $\theta_z$ , because  $v_m$  does increase as the slant increases, but  $I_n$  does not change greatly; the slant causes the magnitude of the normal motion field to increase where  $\Lambda$  is closer to  $O$  and decrease where it is further away, but the increases and decreases occur about equally for the positive and negative parts of the field (see Fig. 3(a)). Thus in all of these cases,  $I_n$  is quite a good estimate of  $v_m$ ; it is always an underestimate, but  $v_m$  can be at most 10% bigger than  $I_n$  in our set of cases.

In Fig. 7, the increase of  $R$  with  $\theta_z$  becomes much larger for larger values of  $\psi_z$ . This is because for these  $\psi_z$ 's the part of  $\Lambda$  for which the normal motion field is negative is closer to  $O$ , so that the negative part of the field has increased magnitude; this causes  $I_n$  to decrease, and  $R$  to increase, more rapidly with  $\theta_z$  for larger values of  $\psi_z$ . Here again,  $I_n$  is always an underestimate of  $v_m$ ; and  $v_m$  can be bigger than  $I_n$  by as much as 75%. In Fig. 8, on the other hand, the slant causes the positive part of the field to have increased magnitude, so that  $I_n$  increases rapidly, especially for larger values of  $\psi_z$ ; this causes  $R$  to decrease, and to actually become less than 1, as  $\theta_z$  increases. In other words, for these cases  $I_n$  becomes an overestimate of  $v_m$ ; but  $v_m$  can be at most 25% smaller than  $I_n$ .

We now examine the bounds on  $R$  given by Eqs. (23) and (24). These bounds depend on the quantities  $\tan \theta_s$ ,  $\Delta\theta_m$ , and  $A_{S_2^p}/A_{S^p}$ , as well as  $\alpha_\sigma$  and  $\alpha_\lambda$ . Here  $\theta_s$  is the latitude of a point on  $S$ , and has value  $\cos^{-1}(A_{S^p}/A_S)$  (see Eq. (11)); in our examples it is nearly equal to  $\theta_z$ . The quantity  $\Delta\theta_m$  is the maximum of the difference in latitude between  $\theta_s$  ( $\approx\theta_z$ ) and any point on  $S$  (see Eq. (13)).

As regards  $\alpha_\sigma$  ( $\alpha_\lambda$ ), the variation in the distance to the points on  $\Sigma$  ( $\Lambda$ ), let the perpendicular from  $O$  to  $\Pi_\Sigma$  meet  $\Pi_\Sigma$  at  $Q$ , and let  $\psi_p$  be the angle between the rays  $OP$  and  $OQ$ , where  $P$  is an arbitrary point of  $\Sigma$ ; note that  $\psi_p < \pi/2$ . Then the distance  $\rho_p$  to  $P$  is  $|OP| = |OQ| \sec \psi_p$ . If  $Q$  is inside  $\Lambda$ , the distance to a point on  $\Sigma$  varies between  $|OQ|$  and  $|OQ| \sec \psi_{\max}$ , where  $\psi_{\max}$  is the maximum of  $\psi$  for all points on  $\Lambda$ ; hence  $\alpha_\sigma = \sec \psi_{\max} - 1$  (note that  $\alpha_\lambda$  may be smaller than this). If  $Q$  is outside  $\Lambda$ , the distance varies be-

Table 1.  $\alpha_\sigma$  for different combinations of  $|\psi_z|$  and circle size.

$ \psi_z $	Contour size		
	1	3	6
$0^\circ$	0.0002	0.0014	0.0055
$30^\circ$	0.0176	0.0537	0.1100
$45^\circ$	0.0250	0.0769	0.1596
$60^\circ$	0.0307	0.0950	0.1996

tween  $|OQ| \sec \psi_{\min}$  and  $|OQ| \sec \psi_{\max}$ , where  $\psi_{\min}$  is the minimum of  $\psi$  for all points on  $\Lambda$ ; hence  $\alpha_\sigma = \alpha_\lambda = \sec \psi_{\max}/\sec \psi_{\min} - 1$ . Note that the distance  $|OQ|$  to  $\Pi_\Sigma$  does not affect the  $\alpha$ s; they depend only on the orientation of  $\Pi_\Sigma$ . Table 1 shows the value of  $\alpha_\sigma$  for  $|\psi_z| = 0^\circ, 30^\circ, 45^\circ$ , and  $60^\circ$  and for the three circle sizes. Note that the values for  $0^\circ$  are much smaller than the other values, since for a nonslanted contour, the distance is nearly constant.

We compute the values of  $\Delta\theta_m$ ,  $A_{S_2^p}/A_{S^p}$ , and  $\alpha_\sigma$  (see Table 1) directly; we then compute the bounds on the right hand sides of (23) and (24) as functions of  $\theta_z$  for the various cases. In each case, the bound in (23) is used for small  $\theta_z$ 's (such that the direction of motion lies inside  $C$ ), and the bound in (24) for large  $\theta_z$ 's. In what follows, we denote the bound in (23) (=the numerator of the bound in (24)) by  $B$ , and the bound in (24) by  $BD^{-1}$ .

In Fig. 10 we compare  $B$  ( $\equiv BD^{-1}$ ) to  $R$  for  $\psi_z = 0^\circ$ . As might be expected, the bound is quite tight for the smallest circle, and increasingly loose for the larger circles (though even for the largest circle,  $B$  overestimates

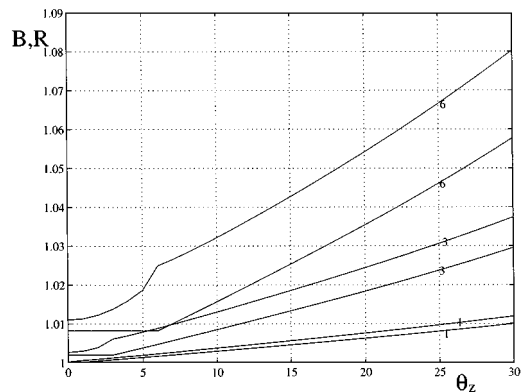


Figure 10. Comparison of  $B$  ( $\equiv BD^{-1}$ ) to  $R$  for  $\psi_z = 0^\circ$ . ( $R$  is the lower curve of each pair.)

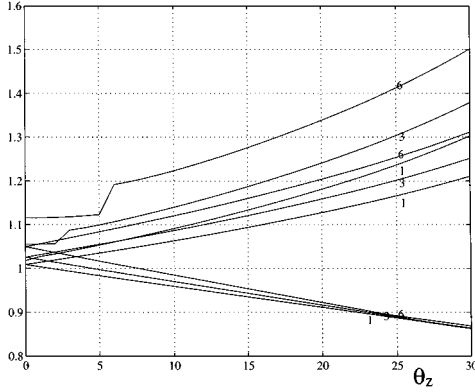


Figure 11.  $B$  and  $BD^{-1}$  compared to  $R$  for  $\psi_z = \pm 30^\circ$  in  $\Pi_0$ . The curves correspond, bottom to top, to  $R$  for  $\psi_z = -30^\circ$ ;  $R$  for  $\psi_z = 30^\circ$ ; and  $B$  and  $BD^{-1}$ .

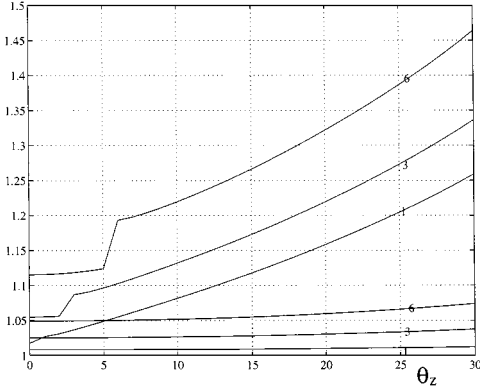


Figure 12.  $B$  and  $BD^{-1}$  compared to  $R$  (the lower set of curves) for  $\psi_z = 30^\circ$  in  $\Pi_1$ .

$R$  by at most  $1/3$ ). The overestimate is due to the fact that  $B$  has  $(1 + \alpha_\sigma)$  as a factor, and  $\alpha_\sigma$  is a worst-case estimate of the variability of  $\rho$  on  $\Sigma$ ;  $I_n$  actually estimates  $v$  at some mean value point of  $\Sigma$  whose distance from  $O$  is (usually) much less than the distance to the points on  $\Lambda$  (=the maximum of the distances to the points on  $\Sigma$ ).

Figure 11 compares  $B$  and  $BD^{-1}$  to  $R$  for  $\psi_z = \pm 30^\circ$  in  $\Pi_0$ . Figure 12 compares them for  $\psi_z = 30^\circ$  in  $\Pi_1$ . In Fig. 11 we see that for the positive  $\psi_z$ 's the  $B$  curves roughly approximate the  $R$  curves, this is because for these  $\psi_z$ 's,  $I_n$  is an underestimate of  $v_m$ , so that  $R$  is greater than 1. For the negative  $\psi_z$ 's, on the other hand, as remarked in connection with Fig. 8,  $R$  is less than 1, and similarly in Fig. 11, as remarked in connection with Fig. 9,  $R$  is approximately 1; thus in these two sets of cases, the bounds are very loose. Again, this is not surprising, because the bounds are based on worst-case

assumptions about the variability of  $\rho$  on  $\Sigma$  (and  $\Lambda$ ). The discontinuities in the graphs (cf. Figs. 11 and 12) are due to the fact that the FOE moves from inside to outside the contour, so that different bounds must be used.

## 6. Experiments

This section shows how our methods can be applied to planar images of real motion sequences.

### 6.1. Planar and Spherical Normal Flow

Let  $I(x, y, t)$  be the plane image intensity function. The time derivative of  $I$  can be written as

$$\frac{dI}{dt} = \nabla I \cdot \dot{\vec{r}} + I_t$$

where  $\nabla I$  is the image gradient and the subscripts denote partial derivatives.

If we assume  $dI/dt = 0$ , i.e., that the image intensity does not vary with time, then we have  $\nabla I \cdot \vec{u} + I_t = 0$ . The vector field  $\vec{u}$  in this expression is called the *optical flow*. The component of  $\vec{u}$  in the image gradient direction  $\vec{n}_r \equiv \nabla I / \|\nabla I\|$  is

$$\vec{u}_n = (\vec{u} \cdot \vec{n}_r) \vec{n}_r = \frac{-I_t \nabla I}{\|\nabla I\|^2} \quad (25)$$

and is called the *normal flow*.

It was shown in (Verri and Poggio, 1987) that the magnitude of the difference between  $\vec{u}_n$  and the normal motion field  $\vec{r}_n$  is inversely proportional to the magnitude of the image gradient. Hence  $\vec{r}_n \approx \vec{u}_n$  when  $\|\nabla I\|$  is large. Equation (25) thus provides an approximate relationship between the 3-D motion and the image derivatives at points where  $\|\nabla I\|$  is large. We use this approximation in this paper.

Since we have used spherical coordinates in this paper we now show how the spherical perspective normal flow can be computed from the plane perspective normal flow. Assuming that the focal length is unity and that the image center is at  $(0, 0)$ , for every point  $x = \cos \varphi \tan \theta$ ,  $y = \sin \varphi \tan \theta$  we have  $I(x, y, t) = I^s(\theta, \varphi, t)$  ( $I^s$  is the spherical image) and  $\partial I^s / \partial t = \partial I / \partial t$ ; also

$$\begin{aligned} \frac{\partial I^s}{\partial \theta} &= \frac{\partial I}{\partial x} \cdot \frac{\partial x}{\partial \theta} + \frac{\partial I}{\partial y} \cdot \frac{\partial y}{\partial \theta} \\ \frac{\partial I^s}{\partial \varphi} &= \frac{\partial I}{\partial x} \cdot \frac{\partial x}{\partial \varphi} + \frac{\partial I}{\partial y} \cdot \frac{\partial y}{\partial \varphi} \end{aligned}$$

which gives us

$$\begin{pmatrix} \frac{\partial I^s}{\partial \theta} \\ \frac{1}{\sin \theta} \frac{\partial I^s}{\partial \varphi} \end{pmatrix} = \begin{pmatrix} \cos \varphi & \sin \varphi \\ -\frac{\sin \varphi}{\cos^2 \theta} & \frac{\cos \varphi}{\cos^2 \theta} \end{pmatrix} \cdot \begin{pmatrix} \frac{\partial I}{\partial x} \\ \frac{\partial I}{\partial y} \end{pmatrix}. \quad (26)$$

[If the focal length is not unity or the image center is not at  $(0, 0)$  the image coordinates must be transformed. If  $(i, j)$  are pixel coordinates in the planar image, the image coordinates are  $x = (i - i_c)/f$ ,  $y = (j - j_c)/f$ , where  $f$  is the focal length in pixels and  $(i_c, j_c)$  are the pixel coordinates of the optical center of the image.] From Eq. (26) we see how the spatial derivatives in the spherical image can be computed from those in the planar image. The temporal derivatives are the same at corresponding points of the planar and the spherical images. We can thus compute the spherical normal flow from (25) by substituting the spherical image derivatives for the planar image derivatives. [Alternatively, we could compute the spherical normal flow from the plane image normal flow by using the matrix inverse of the Jacobian on the r.h.s. of (26).]

### 6.2. Finding and Tracking Contours

We extracted contours from the planar images using the following procedure:

1. Image gradients were computed, and thresholding was applied to remove the points with small gradient magnitudes.
2. A few “seed” points with high values of the gradient magnitude were selected.
3. A dynamic programming algorithm was applied to connect the seed points and thus obtain closed contours. The cost function used was inversely proportional to the gradient magnitude, and was also proportional to the cosine of the angle between the edge direction and the image gradient direction, so that the edge directions orthogonal to the local gradient direction were assigned low costs.

The contours were converted to the spherical projection using the equations at the beginning of Section 2.1.

The contours were tracked in successive frames (plane images) using the following procedure:

1. Normal flow values were computed for the contour points.

2. Based on normal flow values candidate “successor” points were determined for each contour point; all possible successors were marked.
3. A directed acyclic graph (DAG) was created by connecting the candidate contour points based on their gradient directions.
4. The maximum magnitude path was found in this DAG; the magnitude of each edge in the DAG was the average of the gradient magnitudes at the two ends of the edge.

### 6.3. Experiment 1: Indoor Sequence

This sequence was provided by NASA Ames Research Center; it consists of 151 frames, each  $512 \times 512$  pixels. The motion is forward translation ( $\vec{\Omega} \approx \vec{0}$ ) and the FOE is at  $(232, 248)$ , on the coke can at the center of the images. Figure 13 displays several frames from this sequence. Five contours  $C_1, C_2, C_3, C_4,$  and  $C_5$  (see Fig. 14) were extracted from the first frame and

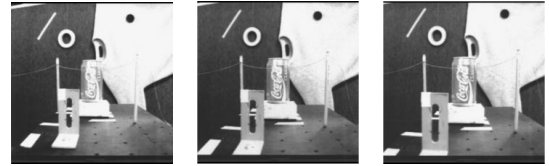


Figure 13. Frames 0, 40, and 80 of the indoor sequence.

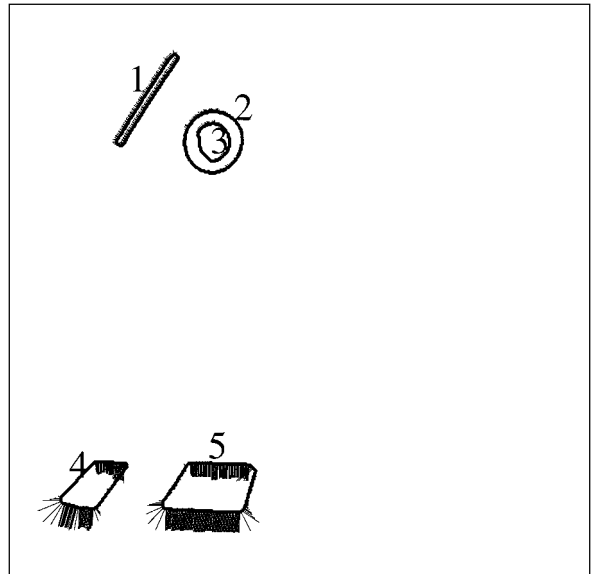


Figure 14. The normal flow for the five contours extracted from the first frame of the indoor sequence.

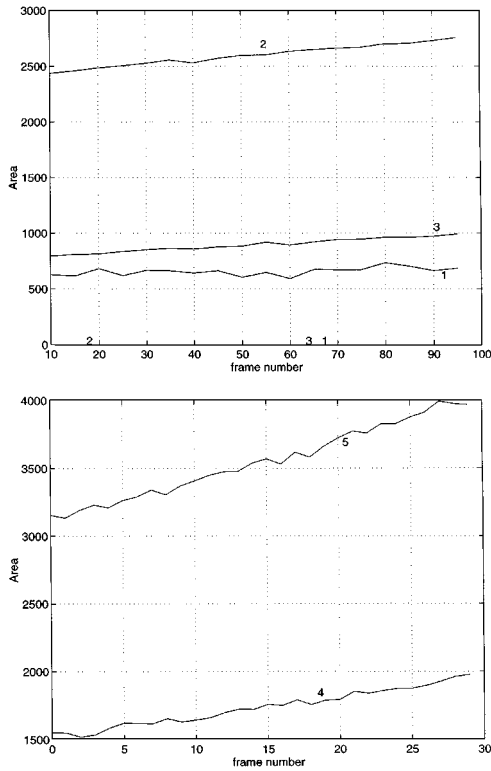


Figure 15. Areas enclosed by the five contours.

tracked using the procedures described in Section 6.2. Contours  $C_4$  and  $C_5$  were tracked in the first thirty frames only since they are not fully visible in the later frames. The areas of the five contours are plotted (as functions of frame number) in Fig. 15. As can be seen, these areas increase approximately linearly.

We computed the normal flow in spherical coordinates using Eqs. (25) and (26); we then computed the integral  $\int_C u_n dl$  of the normal flow around each contour, and divided it by  $2A_S$  to obtain  $I_n$  which is used as an estimate of the ROA. The results for the five contours are shown in Figs. 16 and 17.

The time interval between frames was taken as unity so that the ROA is measured as the fraction of the object-camera distance traveled between each frame and the next. The sequence was collected in a stop-and-shoot mode, and the steps were apparently not equal, so that the motion was not smooth. This is confirmed by our experiments which show consistent variability in the values of  $I_n$ , computed from each set of contours ( $C_1, C_2, C_3$  and  $C_4, C_5$ ).

No information about the 3-D positions of the objects in the scene was provided. Contours  $C_1, C_2$  and  $C_3$  arise from the ‘‘pencil’’ and ‘‘ring’’ shapes on the back

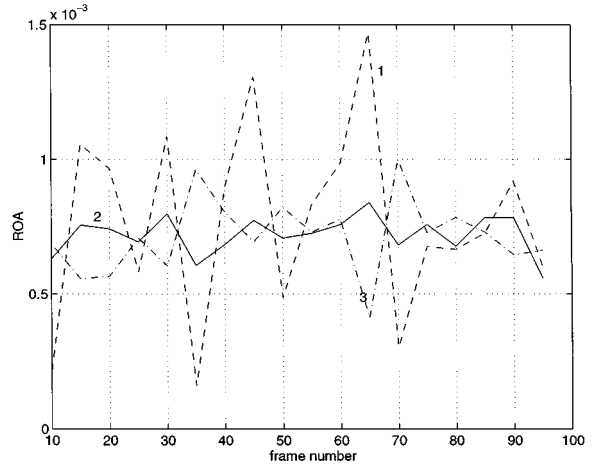


Figure 16. The ROA results for contours  $C_1, C_2,$  and  $C_3$  of the indoor sequence.

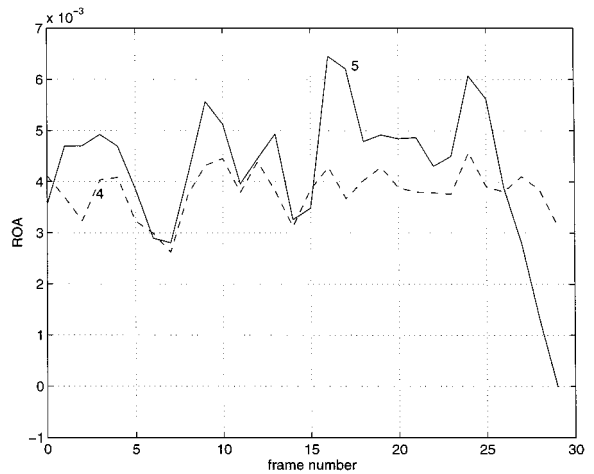


Figure 17. The ROA results for contours  $C_4$  and  $C_5$  of the indoor sequence.

wall. It appears that the wall surface is slightly slanted so that its upper part is slightly more distant from the camera than its lower part. However, the objects giving rise to  $C_1, C_2,$  and  $C_3$  are thick, and the contours are occluding contours. In the case of contour  $C_2$  this compensates for the slant of the wall, so that  $C_2$  is approximately fronto-parallel; this makes  $I_n$  a good estimate of the ROA. In the case of  $C_1$ , the right side of the contour (the side with the inward pointing normal flow) is more distant from the camera than the left side so that  $D_{\hat{\Sigma}}$  (see Eq. (18)) is positive. Furthermore, the ratio  $A_{S_1^p}/A_{S^p}$  is very large (see Table 2) and thus  $D_{\hat{\Sigma}}$  is very large too. As a consequence, although one might think that the ROA for  $C_1$  should be smaller than the ROA for  $C_2$  (because  $C_1$  is angularly farther than  $C_2$

Table 2. Values of  $A_S$ ,  $A_{S_1^p}/A_{SP}$ ,  $A_{S_2^p}/A_{SP}$ ,  $\theta_s$ , and  $\Delta\theta_m$  computed for the five contours from the spherical images at frame 20.

Contour	$A_S$	$A_{S_1^p}/A_{SP}$	$A_{S_2^p}/A_{SP}$	$\theta_s(\text{deg})$	$\Delta\theta_m(\text{deg})$
$C_1$	0.0015	16.7	17.7	$19.2^\circ$	$1.54^\circ$
$C_2$	0.0062	1.3	2.3	$13.1^\circ$	$2.63^\circ$
$C_3$	0.0021	2.6	3.6	$13.1^\circ$	$1.58^\circ$
$C_4$	0.0036	3.3	4.3	$26.1^\circ$	$3.02^\circ$
$C_5$	0.0083	2.8	3.8	$21.5^\circ$	$3.03^\circ$

from the FOE, and the pencil is farther from the camera than the ring), in fact, it varies more and is larger almost everywhere. In the case of  $C_3$  the occluding contour increases (rather than canceling, as it did for  $C_2$ ) the slant of the wall. As a consequence  $D_{\hat{\xi}}$  is negative so that it lowers the value of the ROA. Since the value of  $A_{S_1^p}/A_{SP}$  is higher than for  $C_2$  the computed value of  $I_n$  varies more in the case of  $C_3$  than in the case of  $C_2$ , as can be seen from Fig. 16. Furthermore, because  $D_{\hat{\xi}}$  has opposite signs for the two contours,  $I_n$  varies in opposite ways.

In the case of  $C_4$  and  $C_5$  the estimated ROA for the two contours is approximately the same, but somewhat smaller for  $C_4$  because of its greater distance from the camera and higher value of  $\theta_s$ . (For both of these contours the occluding contour effect reinforces the slant of the table top.) However, the greater variability of the distance, and consequently the higher value of  $\alpha_\lambda$ , in the case of  $C_5$  make the estimated ROA vary more for  $C_5$  than for  $C_4$ . Note that the pieces of these two contours for which the normal flow is negative are more distant from the camera than the pieces for which the normal flow is positive. Thus  $D_{\hat{\xi}}$  is positive and large, and as a consequence  $I_n$  overestimates the ROA.

#### 6.4. Experiment 2: Outdoor Sequence

This sequence was provided by IRISA and Thomson LER Cesson-Seigné. It consists of 66 frames, each  $288 \times 332$  pixels. The camera is carried by a moving vehicle which follows a van. Figure 18 displays several frames from this sequence. Two contours

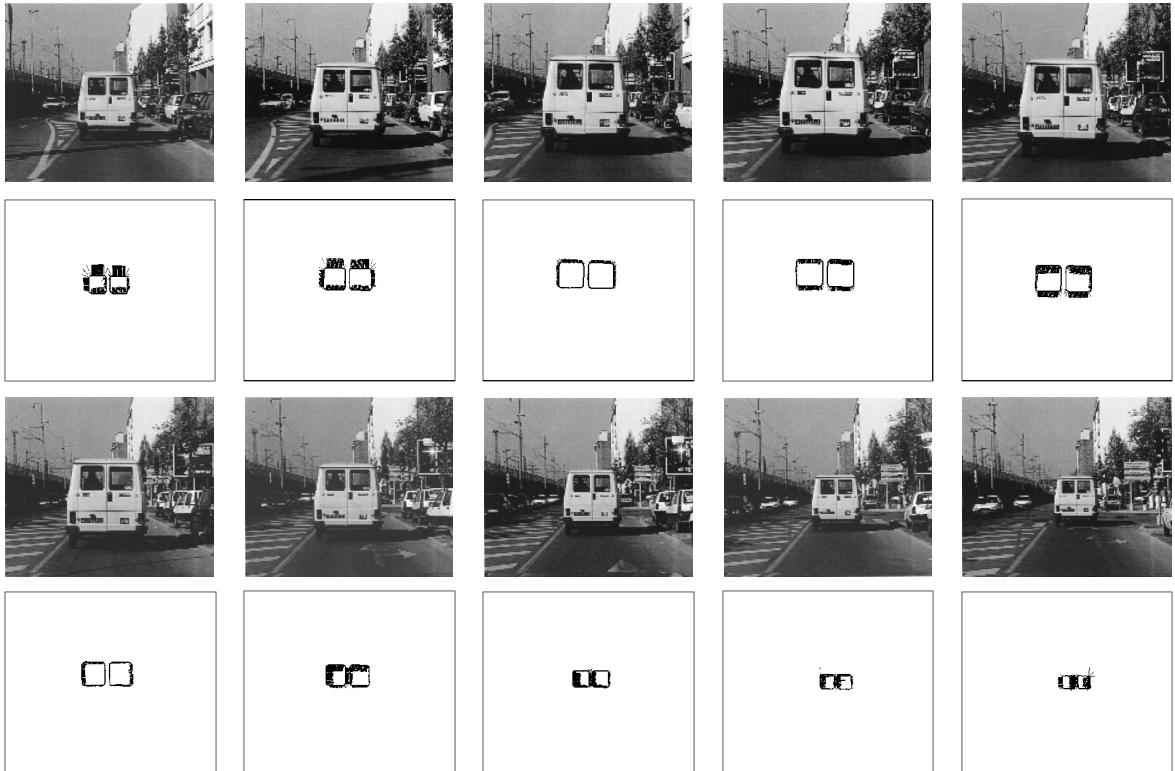


Figure 18. Frames 5, 10, 15, 20, 25, 30, 35, 40, 45, and 50 of the outdoor sequence. The second and fourth rows contain corresponding normal flow images.

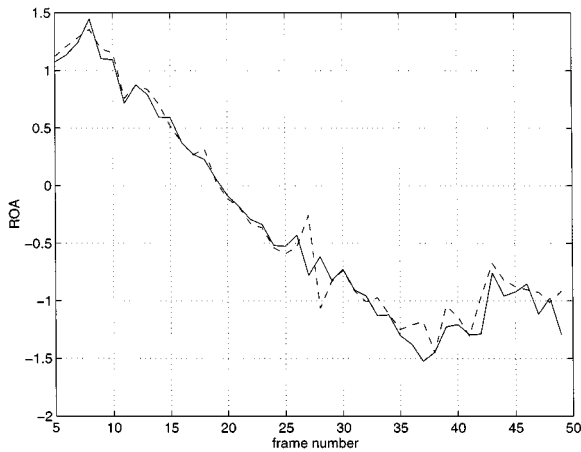


Figure 19. The ROA results for the outdoor sequence. The solid line corresponds to the left window of the van and the dashed line corresponds to the right window. The ROA decreases steadily between frames 7 and 37; it becomes negative at frame 20.

corresponding to the left and right back windows of the van (see Fig. 18) were extracted from the fifth frame and tracked in the next 45 frames by the procedures described in Section 6.2. Figure 19 displays the estimated ROAs (in units of fraction of distance per second) for these contours, which are angularly close to the FOE and approximately frontal. As can be seen from Fig. 18 the van is getting closer to the camera at first, but then it starts moving away. At frame 19 the relative speed is zero; afterwards, the van pulls away from the vehicle carrying the camera. We obtain very similar results for the two windows except at frames 27 and 28 when a shadow passes over the right window of the van. However, our program recovers from this event and continues to track the contours.

## 7. Conclusions

We have used Green's theorem and the mean value theorem to derive Eq. (8), which relates the average value of  $v$  (the rate of approach, ROA), and the integral of the partial derivative (with respect to  $\theta$ ) of the distance of a 3-D surface patch  $\Sigma$ , to the integral  $I_n$  of the normal motion field along the boundary  $C$  of the spherical image of  $\Sigma$  (Section 3). We have derived upper bounds on  $R = v/I_n$  (Section 4), and have quantitatively studied the behavior of  $R$  and these bounds for a class of examples (Section 5). We have also verified our analysis qualitatively for two real image sequences (Section 6). This paper illustrates how it is possible to derive bounds on the estimates of quantities such as

the ROA under given assumptions about the geometry of the scene. In this paper we have derived only upper bounds, which are the critical bounds as regards obstacle avoidance; but a similar analysis could have been used to derive lower bounds. Our experiments using real data show that contour integrals in an image are a useful source of information about the ROA, which can in turn be used for looming detection and obstacle avoidance.

Now that there exist a substantial number of algorithms that compute the ROA and the TTC, it would be interesting to compare them on common data sets. However, since most of the other papers on the subject present results only on a few images, while others require substantial motion between frames, or make other assumptions about the type of motion, it was not feasible to present a comparative analysis in this paper. The comparison of various methods of computing the ROA is one of our future research goals.

## Notes

1. It can be computed using the method described in (Aloimonos and Duric, 1994).
2. This can be done since  $\bar{s}(\varphi) \geq 0$ .

## References

- Adiv, G. 1985. Determining three-dimensional motion and structure from optical flow generated by several moving objects. *IEEE Transactions on Pattern Analysis and Machine Intelligence*, 7:384–401.
- Albus, J.S. 1991. Outline for a theory of intelligence. *IEEE Transactions On Systems, Man, and Cybernetics*, 21:473–509.
- Aloimonos, Y. and Duric, Z. 1994. Estimating the heading direction using normal flow. *International Journal of Computer Vision*, 13:33–56.
- Ancona, N. and Poggio, T. 1993. Optical flow from 1D correlation: Application to a simple time-to-crash detector. In *Proc. ARPA Image Understanding Workshop*, pp. 673–682.
- Atkinson, K.E. 1989. *An Introduction to Numerical Analysis*. John Wiley and Sons: New York.
- Bruss, A. and Horn, B.K.P. 1983. Passive navigation. *Computer Vision, Graphics, and Image Processing*, 21:3–20.
- Burlina, P. and Chellappa, R. 1996. Analyzing looming motion components from their spatiotemporal spectral signature. *IEEE Transactions on Pattern Analysis and Machine Intelligence*, 18:1029–1034.
- Burlina, P. and Chellappa, R. 1998. Temporal analysis of motion in video sequences through predictive operators. *International Journal of Computer Vision*, 28:175–192.
- Cipolla, R. and Blake, A. 1992. Surface orientation and time to contact from image divergence and deformation. In *Proc. European Conference on Computer Vision*, pp. 187–202.

- Francois, E. and Bouthemy, P. 1990. Derivation of qualitative information in motion analysis. *Image and Vision Computing*, 8:279–288.
- Horn, B.K.P. and Schunck, B.G. 1981. Determining optical flow. *Artificial Intelligence*, 17:189–203.
- Ikeuchi, K. 1984. Shape from regular patterns. *Artificial Intelligence*, 22:49–75.
- Koenderink, J.J. and Van Doorn, A.J. 1975. Invariant properties of the motion parallax field due to the movement of rigid bodies relative to an observer. *Optica Acta*, 22:773–791.
- Lee, D.N. 1980. The optical flow field: The foundation of vision. *Phil. Trans. Royal Society London*, B 290:169–179.
- Longuet-Higgins, H.C. and Prazdny, K. 1980. The interpretation of a moving retinal image. *Proc. Royal Society London*, B 208:385–397.
- Marsden, J.E. and Tromba, A.J. 1976. *Vector Calculus*, W.H. Freeman and Company: San Francisco.
- Maybank, S.J. 1987. Apparent area of a rigid moving body. *Image and Vision Computing*, 5:111–113.
- Meyer, F. and Bouthemy, P. 1992. Estimation of time-to-collision maps from first order motion models and normal flows. In *Proc. 11th Int. Conf. on Pattern Recognition*, pp. 78–82.
- Nakayama, K. 1985. Biological image motion processing: A review. *Vision Research*, 25:625–660.
- Nelson, R.C. and Aloimonos, J. 1989. Obstacle avoidance using flow field divergence. *IEEE Transactions on Pattern Analysis and Machine Intelligence*, 11:1102–1106.
- Poggio, T., Verri, A., and Torre, V. 1991. Green theorems and qualitative properties of the optical flow. A.I. Memo 1289. MIT: Cambridge, MA.
- Sharma, R. 1992. Active vision in robot navigation: Monitoring time-to-collision while tracking. In *Proc. IEEE/RSJ International Conference on Intelligent Robots and Systems*.
- Subbarao, M. 1990. Bounds on time-to-collision and rotational component from first-order derivatives of image flow. *Computer Vision, Graphics, and Image Processing*, 50:329–341.
- Tistarelli, M. and Sandini, G. 1993. On the advantages of polar and logpolar mappings for direct estimation of time-to-impact from optical flow. *IEEE Transactions on Pattern Analysis and Machine Intelligence*, 15:401–410.
- Verri, A. and Poggio, T. 1987. Against quantitative optical flow. In *Proc. International Conference on Computer Vision*, pp. 171–180.